KINETIC MONTE CARLO SIMULATION OF MBE GROWTH OF LAYERED HEXAGONAL BORON NITRIDE

A Thesis

Presented to the Faculty of the Graduate School

of Cornell University

In Partial Fulfillment of the Requirements for the Degree of

Master of Science

by

Ren Zhong

August 2019

ABSTRACT

Hexagonal boron nitride (hBN) is a two-dimensional atomically thin semiconductor material. It is expected to exhibit fascinating electronic, photonic, and thermal properties. To obtain atomically thin monolayers, chemical vapor deposition (CVD) and molecular beam epitaxy (MBE) has been employed to grow hBN on different substrates. However, the high density of grain boundaries and other defects limit the potential of hBN. A deep understanding of the physics of crystal growth, facilitated by the substrate surface in an MBE environment is necessary to improve the synthesis technique for high-quality hBN.

In this work, we have analyzed the hBN deposition and diffusion process using Nudged Elastic Band, and the transition state theory. A Kinetic Monte Carlo (KMC) model is constructed to simulate hBN MBE growth under various temperatures, flux ratios, and flux rates. The model is calibrated with experimental data and has produced reliable predictions of hBN growth dynamics, propensities to form various geometric configurations, growth rates, and nucleation properties. In addition, the model captures the influence of input N isotope (N^{14} and N^{15}) ratios and the number of layers on hBN Raman spectra. A Raman peak shift, from 1359 cm^{-1} (100% N^{14}) to 1339 cm^{-1} (100% N^{15}), has been observed. It is found that increasing the deposition thickness will lead to transitions of hBN Raman peaks. The KMC model developed here and the findings of this study for hBN should prove useful to a wider class of 2D materials.

BIOGRAPHICAL SKETCH

Ren Zhong is a Master of Science student from the Department of Materials Science and Engineering, Cornell University. He graduated from Hong Kong Polytechnic University with a B.S. in Engineering Physics in 2017. His research interests include theoretical modeling and simulation of the growth process as well as the physical properties of thin film materials.

For Rachel and my family

ACKNOWLEDGMENTS

I would like to express my sincere gratitude to:

Prof. Debdeep Jena and Prof. Huili Grace Xing, for accepting me to work in this fantastic group, providing me invaluable advices for my research, and encouraging me to overcome all the obstacles.

Dr. Guru Khalsa, Dr. Yongjin Cho, Ryan Page, Nicholas Tanen, and Nima Leclerc, for your generous help and guidance, as well as your patience to all my questions.

Rachel, my family, and my friends, for supporting me in the deepest darkness. I could not reach this point without your understanding and inspiration.

PARADIM, XSEDE, ICSE, for providing computational resources for my research.

TABLE OF CONTENTS

LIST OF FIGURES

LIST OF TABLES

LIST OF ABBREVIATIONS

AFM	Atomic Force Microscope
B	Boron
CVD	Chemical Vapor Deposition
DFT	Density Functional Theory
KMC	Kinetic Monte Carlo
MBE	Molecular Beam Epitaxy
MD	Molecular Dynamics
MEP	Minimum energy path
ML	Monolayer
N	Nitrogen
NEB	Nudged Elastic Band
NN	Nearest neighbor
PBE	Perdew-Burke-Ernzerhof
QM	Quantum Espresso
SNN	Second nearest neighbor
TSK	terrace-step-kink
XC	exchange-correlation
hBN	hexagonal Boron Nitride
hcp	hexagonal close packed
vc	variable-cell
2D	two dimensional

CHAPTER 1

INTRODUCTION

1.1 Layered hexagonal Boron Nitride (hBN) properties and applications

Since the exfoliation of the single layer graphene in 2004 [1], two dimensional (2D) materials have attracted tremendous research interest in their structure, properties and potential applications [2]–[4]. Many other 2D materials, such as MoS_2 [5], WSe_2 [6] and Borophene [7], were gradually discovered and studied in the following years.

Hexagonal boron nitride (hBN) is a two dimensional atomically thin semiconductor material, which exhibits many fascinating properties. Many studies have presented the utilization of its flexoelectricity [8], optical hyperbolicity [9] and atomically flat surface [10] in creating new applications. In addition, due to the strong covalent sp^2 BN bonds, hBN is reported to have high thermal conductivity, as well as outstanding chemical and temperature stability [11].

The unique electronic and optical properties of hBN have been used in inventing new electronic devices. Jiang and Lin [12] reported an exploitation of a novel emitter layer structure based on hBN and AlGaN p-n junction (**Fig 1.1(a)**), which can produce 225 nm deep ultraviolet light. Tran et al. [13] investigated the quantum emission effect from defects in single-crystalline hBN and constructed single photon emitter with an emission

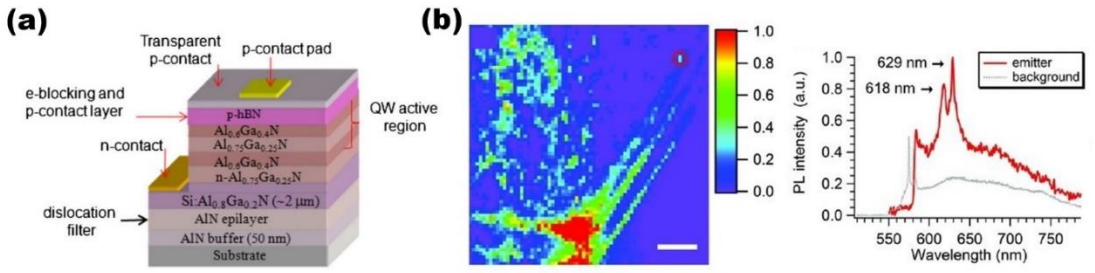

Figure 1.1 ***(a)*** *Schematic of a novel deep ultraviolet light emitting diode layer structure using p-type hBN* [12] ***(b)*** *A typical confocal map showing isolated emission centers and ensembles of the single photon emitters using hBN. The scale bar indicates 10 μm.* [13]

band at approximately 770–900 nm **(Fig 1.1(b))**. Ahmed et al. [14] achieved a thermal neutron detector by growing hBN on the vertical (111) surfaces of parallel trenches fabricated in (110) Si.

1.2 hBN and Graphene heterostructure

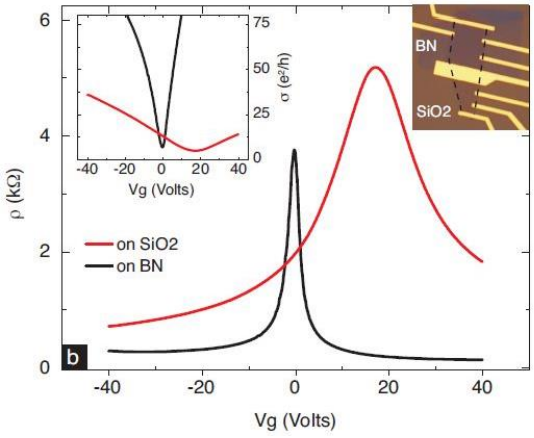

Figure 1.2 *Resistivity measured on a graphene single flake spanning both BN and SiO_2 substrate regions.* [15]

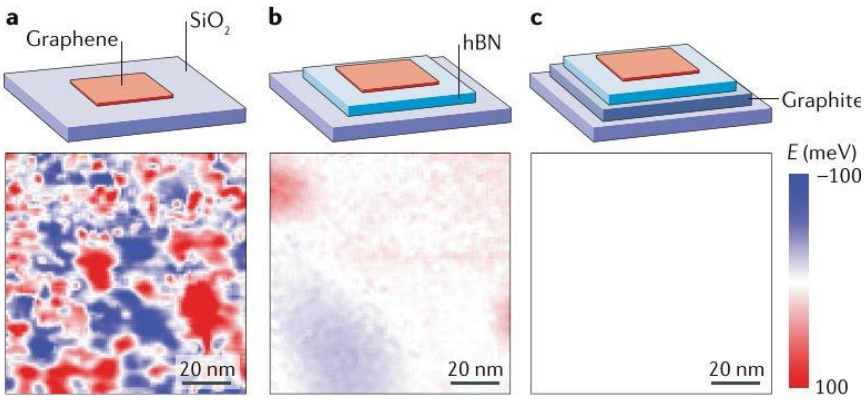

Figure 1.3 *The schematics show the structures of different devices (SiO_2 substrate, hBN substrate, and Graphite-hBN substrate) and charge fluctuations measured by scanning tunneling spectroscopy in each device* [16]

The atomically thin flakes of 2D materials can be mixed into heterostructures with new electronic and optical properties [17]. The lattice mismatch between hBN and graphene is only 1.7%, which makes hBN a desirable complementing material for graphene to create new devices. [18], [19] Graphene encapsulated in hBN substrate is reported to have high electron mobility [20], with very low surface trapped charge [21]. As shown in **Fig 1.2**, the electron mobility of graphene film measured on an hBN substrate is significantly lower than the values for devices fabricated on SiO_2. [15] In addition, well-developed multicomponent integer and fractional quantum Hall effect are detected in the high mobility hBN-graphene devices. [16] It is also reported that graphene devices grown on hBN substrate experiences dramatically low charge inhomogeneity, due to the atomically smooth surface of hBN [22]. **Fig 1.3** shows that the charge fluctuation of graphene-hBN device three orders of magnitude lower than graphene-SiO_2 device. [16]

1.3 Growth methods and their limitations

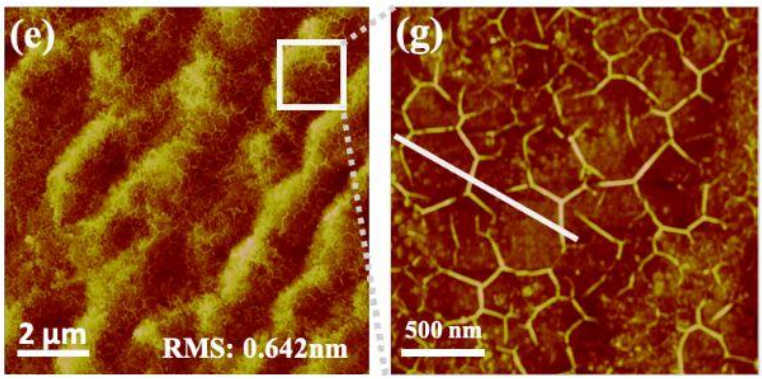

Figure 1.4 *AFM images of rotationally aligned hBN on sapphire substrate grown by MBE* [23]

The potential utilization of 2D materials, like hBN, require the development of stable and controllable growth methods. Except for mechanical exfoliation, many other synthesis methods are being studied to effectively produce hBN atomic layers. As shown in **Fig 1.4**, Page et al. [23] reported the growth of smooth, layere, few-nanometer hBN films on a nitridated sapphire under 1600°C using Molecular Beam Epitaxy (MBE). Paduano et al. [24] indicated that highly uniform hBN films were successfully grown on sapphire substrate by Metal Organic Chemical Vapor Deposition (MOCVD). It is demonstrated by Park et al. [25] that the plasma-enhanced Atomic Layer Deposition (ALD) was used to produce atomically smooth and scalable hBN films, with low leakage current density and reasonable dielectric constant.

However, the control of structural properties remains a huge difficulty that prevents us to obtain high quality hBN. **Fig 1.5** shows some of the typical defects in hBN growth,

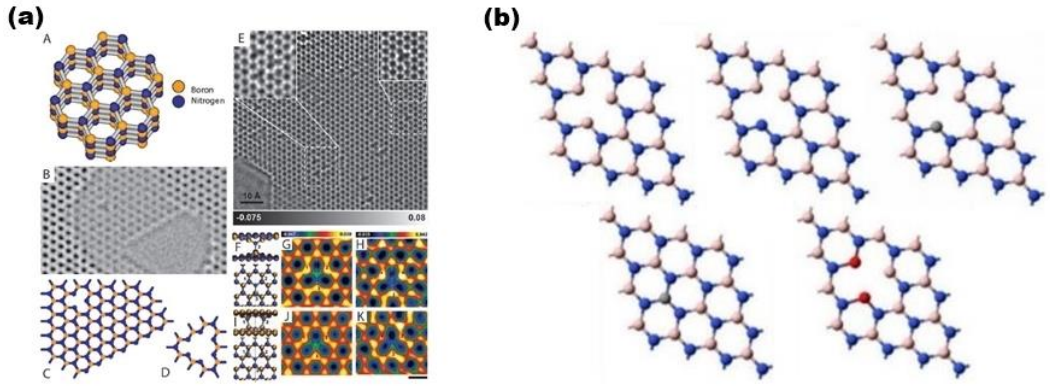

Figure 1.5 ***(a)*** *Atomic defects in hBN* [26] ***(b)*** *Defects structures identified in CVD-grown hBN* [27]

including atomic vacancy, impurity, high density grain boundary, etc [26], [27]. Since the relationship between experimental conditions and microscopic growth kinetics is complicated, it is usually time-consuming to optimize growth parameters with experimental techniques. To solve these problems, computational simulation is an important method to understand the growth mechanism of hBN and therefore achieve high quality controllable synthesis.

1.4 Kinetic Monte Carlo Methods and Transition State Theory

The first principle method based on density functional theory (DFT) is a widely used simulation tool for 2D materials [28], [29]. The DFT method is capable of accurately predicting fundamental structural and electronic properties of materials. However, this method is limited to modeling static processes within a microscopic time range [30], but

not dynamic processes in a long time interval, such as material growth. Another challenge of using DFT is that the growth model requires an open system with proper representation of atom addition and subtraction.

To overcome these challenges, the kinetic Monte Carlo (KMC) method was adapted to simulate the non-equilibrium kinetic evolution of 2D materials [31]. Whitesides and Frenklach [32] modeled the graphene-edge evolution under various temperature, gas-phase composition, and reaction rates conditions with KMC method. A lattice-based diffusion KMC model was constructed by Nie et al. [33] to simulate the synthesis process of WSe_2. Govind Rajan et al. [34] employed the KMC model to understand the domain shape evolution of 2D transition metal dichalcogenide (TMD) monolayers grown by CVD. These simulations not only predicted the physical properties of 2D materials but also revealed the atomic level synthesis mechanisms that are hard to be clarified in experiments [35]. However, all the mentioned simulations neglected the influence of substrate, which is a key factor that impacts the electronic properties [36] and surface morphologies [35] of synthesized 2D materials in real growth.

In order to develop a more realistic hBN growth model, we combined a lattice based KMC model with the first principle calculations for more accurate energy barriers for atomic movements. The DFT method takes substrate types, as well as chemical interactions between substrate and deposited hBN films into consideration, which built a theoretical bridge between the statistical method with atomic reactions in experimental studies.

1.5 Raman spectroscopy and isotopic effect of semiconductor

Raman spectroscopy is a characteristic technique used to measure the vibrational modes of materials. This method has been widely exploited in characterizing and studying two dimensional materials, such as graphene and TMDs. In the case of graphene, Raman signatures are used to identify the thickness of single and few-layer graphene films, by comparing the relative intensity of its G and 2D bands [37]. MoS_2, a famous TMD material, also experiences Raman frequency changes in A_{1g} and E_{2g} modes, when reduced to atomically thin layers. [38] Moreover, Raman spectroscopy has been used to examine strain [39], doping [40] and edge state [41] of 2D materials.

The semiconductor materials with controlled isotopic composition have attracted intense interest in recent years. Many important physical properties, including bandgaps [42], thermal conductivity [43] and spin effect [44] are affected by the isotopic composition. For BN, the isotope effect of B^{10} and B^{11} has been studied in many groups. Vuong et al. [45] reported that the varied atom mass of B affects the electronic bandgap and phonon energy of hBN. Han et al. [46] investigated BN nanotubes fabricated with B isotopes, and observed the red shift and peak broadening on radiative transition spectra due to the isotopic effect.

The isotopic hBN can be characterized by Raman spectroscopy, because the atomic mass change results in the Raman peak shifts. However, as mentioned before, the thickness of 2D materials also influences the location and intensity of Raman peaks. It

is difficult to determine the exact isotopic composition of hBN with unknown thickness or vice versa. Theoretical calculations can be used to simulate the Raman signatures of hBN under various isotopic composition and layers conditions, and also provide a guidance of the usage of Raman spectroscopy to analyse hBN.

1.6 Structure of thesis

In this work, a lattice based KMC model is constructed to simulate the monolayer hBN MBE growth on a graphite substrate. In Chapter 2, we calculated the adsorption, desorption, and diffusion energy barriers of Boron and Nitrogen atoms on graphite. The adatom diffusion sites are analyzed according to the relaxation and optimization of hBN-Graphene heterostructures. The adatom movement energy barriers are calculated using Nudged Elastic Band theory. In Chapter 3, a KMC model of hBN growth on highly ordered graphene lattice is constructed based on the energy barriers calculated in Chapter 2. The evolution of surface morphologies and defect analysis are discussed in this part. The influence of experimental parameters, such as temperature, flux rate, and flux ratio, on the nucleation processes and growth rates is also introduced. In Chapter 4, we explored how the Nitrogen isotopes and layer number affect the Raman peak shift of hBN films on a graphite substrate. The tendency of Raman G band peaks of hBN grown with various Nitrogen isotope ratio is presented. We also investigated the Raman peak shift of multilayer hBN synthesized with different Nitrogen isotopes.

CHAPTER 2

NUDGED ELASTIC BAND CALCULATION OF HBN ADSORPTION, DESORPTION AND DIFFUSION ENERGY BARRIERS WITH DFT

2.1 Relaxation and optimization of hBN – Graphene heterostructure

The first-principle calculations in this study are based on density functional theory (DFT), using the PWscf, PWneb and PHonon code from Quantum Espresso (QM). In this chapter, we identified the relative locations and structures of an hBN-Graphene model and calculated the energy barriers of atom adsorption, desorption, and diffusion during epitaxial growth processes.

The first step of building the molecular model is to determine the hBN-Graphene heterostructure. According to Yankowitz [17], both graphene and hBN are two-dimensional materials with a hexagonal lattice structure, and the interlayer force between graphene and hBN is Van der Waals interaction. Thus, we initialized a bilayer hBN-Graphene model connected with Van der Waals force.

Under the assumption that the system with minimized total energy is at equilibrium state, we drew the total energy map of Boron/Nitrogen adatom on an empty graphene substrate to determine the most stable heterostructure. The total energy E of the many-electron system is calculated by **Eq 2.1**:

$$\mathrm{E} = \int \Psi^{*} \hat{H} \Psi \mathrm{d}\mathbf{r} \tag{2.1}$$

where

$$\widehat{H} = \underbrace{-\sum_i \frac{1}{2}\nabla_i^2}_{I} + \underbrace{\sum_i V_n(\boldsymbol{r}_i)}_{II} + \underbrace{\frac{1}{2}\sum_{i\neq j}\frac{1}{|\boldsymbol{r}_i-\boldsymbol{r}_j|}}_{III} \quad (2.2)$$

where

$$V_n(\boldsymbol{r}_i) = -\sum_I \frac{Z_I}{|\boldsymbol{r}-\boldsymbol{R}_I|} \quad (2.3)$$

The terms in $\widehat{H}$ refer to the kinetic energy of electrons (I), electron-nuclei attraction (II) and electron-electron repulsion (III). In DFT calculations, the total energy calculation is simplified as:

$$\mathrm{E}_{\mathrm{total}}[\{\varphi_i\}] = E_{known}[\{\varphi_i\}] + E_{XC}[\{\varphi_i\}] \quad (2.4)$$

that φ_i represents the single electron wave functions. The known term includes everything can be written in the analytical form: electron kinetic energy and Coulombs interactions (electron-electron, electron-nucleus, nucleus-nucleus). The exchange-correlation (XC) term sums up all quantum mechanical effects which are not included in the known term.

.

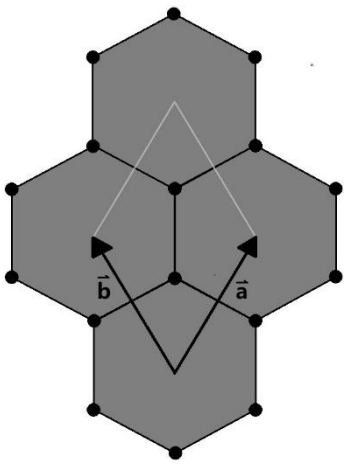

FIGURE 2.1 *Primitive unit cell of graphene*

The total energy calculations are conducted with the help of PWscf code from Quantum Espresso. The plane wave kinetic energy cutoff of the valence electrons is 80 Ry. Exchange correlation energy was treated with the generalized gradient approximation (GGA). The Perdew-Burke-Ernzerhof (PBE) functional was used in combination with Vanderbilt ultrasoft pseudopotentials for B, C and N atoms. The lattice vectors for an orthonormal primitive unit cell (shown in **Fig.2.1**) employed in these calculations were:

$$\vec{a} = a * (\frac{\sqrt{3}}{2}, \frac{3}{2}, 0)$$

$$\vec{b} = a * (-\frac{\sqrt{3}}{2}, \frac{3}{2}, 0)$$

$$\vec{c} = a * (0, 0, \frac{c}{a})$$

where *a* is the C-C bond length in graphene. Integer multiples of $\vec{a}$ and $\vec{b}$ were used for the lateral dimensions of the surface supercells. An equally separated 6x6 grid was generated on a periodic bounded graphene primitive unit cell. By assigning an adatom on one of these grid points, 72 adatom-graphene system models, 36 for Boron and 36 for Nitrogen, were constructed to calculate the total system energy. The lattice constant of graphene primitive unit cell is 2.460 Å and the separation between graphene and adatoms is initialized to be 3.500 Å [47].

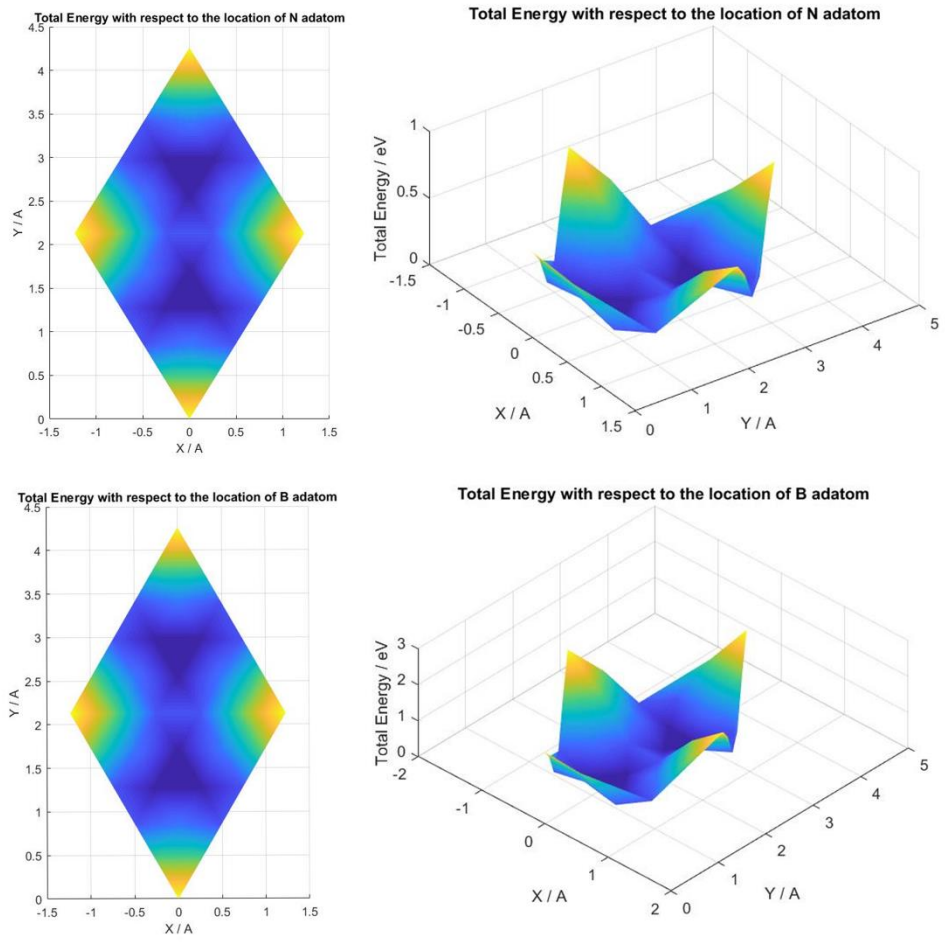

FIGURE 2.2 *Standardized total energy map of Nitrogen/Boron adatoms on a graphene primitive unit cell*

The total energy map of Boron/Nitrogen adatoms on an empty graphene substrate is presented in **Fig.2.2**. Because of the symmetry of graphene primitive unit cell, there are identical minima on the total energy map of each kind of adatom. The minima of total energy of both Boron/Nitrogen systems locate directly upon the carbon atoms, which indicates the model is most stable when the adatoms stay at the on-top sites on the

graphene surface. Therefore, an assumption is made that the free epitaxial atoms tend to stay at the on-top sites on the graphene substrate.

After figuring out the locations of Boron/Nitrogen adatoms on a graphene substrate, the hBN-Graphene model is fully relaxed to its converged structure. Because both of hBN and graphene have hexagonal lattice structure and their lattice mismatch is relatively low (~1.7%) [48], we assumed that there does not exist edge dislocation between graphene surface and layered hBN. Therefore, the initial guess of hBN-Graphene model is constructed by putting 1 Boron and 1 Nitrogen adatoms at the on-top sites of a graphene primitive unit cell. Then, the 'variable-cell (vc) relaxation' is conducted to relax the lattice parameters and atomic positions until the total energy converged to its minimum. The relaxed cell parameters and atomic positions are shown in **Table 2.1** and **Table 2.2**.

	x(Å)	y(Å)	z(Å)
$\vec{a}$	1.243892973	2.154402345	0.000000392
$\vec{b}$	-1.243892973	2.154402345	0.000000392
$\vec{c}$	- 0.000000000	0.000000694	19.996193857

TABLE 2.1 *Relaxed hBN-Graphene unit cell model cell parameters*

	x(Å)	y(Å)	z(Å)
N	-0.000000000	1.436241054	13.586728172
B	0.000000000	2.872493874	13.586739301
C	-0.000000000	1.436280259	9.408958565
C	0.000000000	2.872602692	9.408821401

TABLE 2.2 *Relaxed hBN-Graphene unit cell model atomic positions*

2.2 Epitaxial growth processes and diffusion sites analysis

With the relaxed unit cell model, we simulated the monolayer hBN epitaxial growth process and analyzed all possible surface diffusion configurations.

For the relaxed model, it is assumed that both adsorption and diffusion sites locate at the on-top sites on the graphene surface. Therefore, we constructed the monolayer hBN-Graphene model, which is presented in **Fig.2.3**. Half of the on-top sites on graphene are labeled as Boron-sites and the other half are labeled as Nitrogen sites. These sites are equally separated according to the relaxed model. An adsorbed Boron adatom can only occupy a Boron site and vice-versa. Boron on Nitrogen site as well as Nitrogen on Boron site configurations are not allowed in this model.

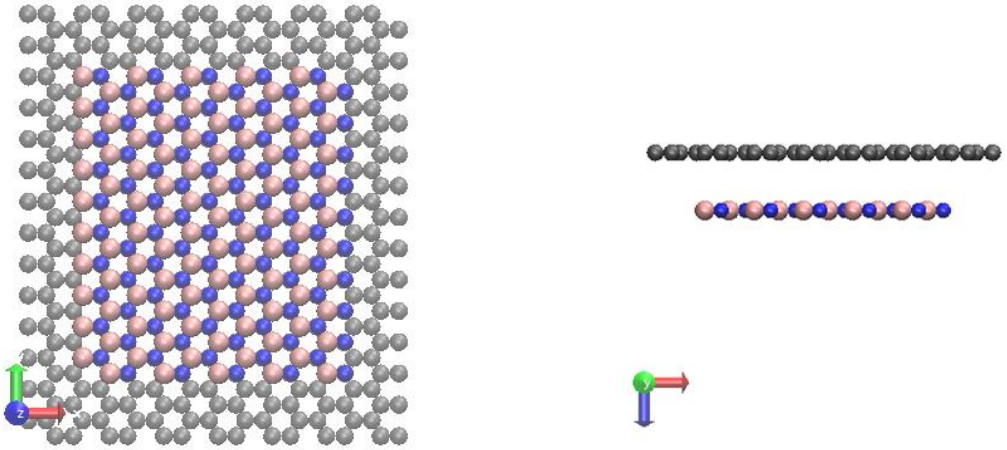

FIGURE 2.3 *The hBN deposition model, consisting of Boron (pink), Carbon (grey), and Nitrogen(blue) atoms* ***(a)*** *Top view of deposited hBN on graphene substrate.* ***(b)*** *Cross section view of deposited hBN on graphene substrate*

The possible movements of adatoms on substrate were classified as adsorption, desorption, and diffusion. These movements were considered to take place at the graphene surface. Bulk diffusion and island migration were neglected. Starting from an empty and flat graphene surface, Boron and Nitrogen atoms are deposited on randomly chosen sites of their own kind. A constant interval between atoms dropping is set to simulate a constant deposition rate. When an adatom arrives a random site, its kinetic energy was neglected.

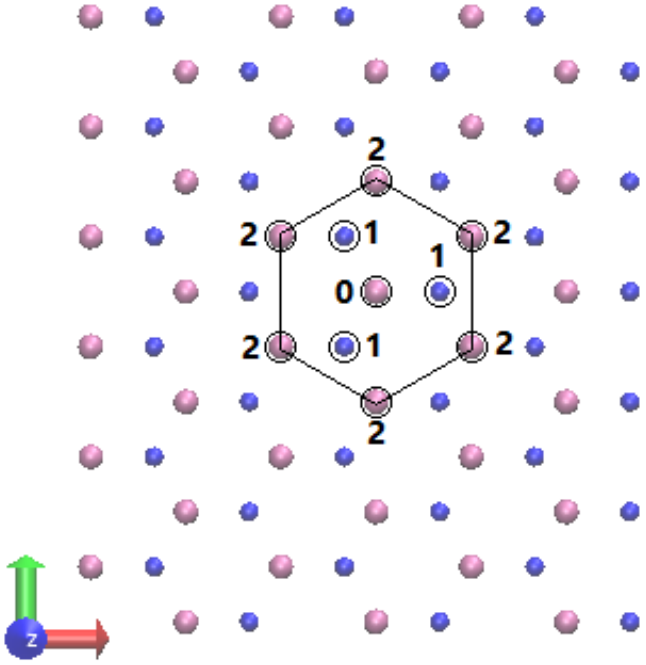

FIGURE 2.4 *Top view of a hBN surface, showing the Boron (pink) and Nitrogen (blue) atoms. If site '0' represents the deposition site, the nearest neighbor (NN) and second nearest neighbor (SNN) are labelled as '1' and '2' respectively*

After being adsorbed on the graphene surface, adatoms have two possible movement types: diffusion and desorption. In **Fig.2.4**, we show an example the microscopic structure of a Boron site (labelled as '0'), including its nearest neighbor (NN, Nitrogen sites, labelled as '1') and second nearest neighbor (SNN, Boron sites, labelled as '2'). In 2D hBN structure, a Boron adatom can form three B-N bonds with its nearest Nitrogen adatom. Therefore, the number of occupied NN sites can be used to represent the number of B-N bonds connecting to the selected adatom. In addition, we assume that in each diffusion step, the adatom can move to one of the nearest empty sites of its

own kind, which are the SNN sites presented in **Fig 2.4**. If an adatom's NNs are empty, i.e. it does not form B-N bond with its nearby adatoms, it has a possibility to desorb from the surface. The desorbed atoms will be removed from the system. In addition to desorption process, Nitrogen atoms may form nitrogen molecules and evaporate from the surface. This movement has also been simulated in the model. Surface diffusion is another kind of movement, which is modeled by the random thermal hopping of surface atoms from one lattice site to one of its empty SNN site. The surface diffusion rate is calculated according to the Arrhenius equation (**Eq 2.5**) based on transition state theory:

$$r = \nu_0 \exp\left(-\frac{E_B}{k_B T}\right) \tag{2.5}$$

The attempt frequency, ν_0, which correspond to the phonon frequency of an atom in a solid. For hBN, the prefactor is chosen as 10^{12} s^{-1} for both Boron and Nitrogen atoms. E_B is the barrier energy that an atom has to climb in order to hop to another site. k_B is the Boltzmann constant and T is the growth temperature at the substrate surface.

The energy barrier is the key factor affecting the diffusion rates. According to the transition state theory, the barrier energy is highly sensitive to the configuration around the site, because the bond breaking and bond formation are the major sources of energy hills. In the hexagonal structure of hBN, one Boron/Nitrogen atom 3 NN sites and 6 SNN sites. Thus, a Boron/Nitrogen atom can form up to 3 Boron-Nitrogen bonds and can diffuse to one of the 6 possible SNN sites.

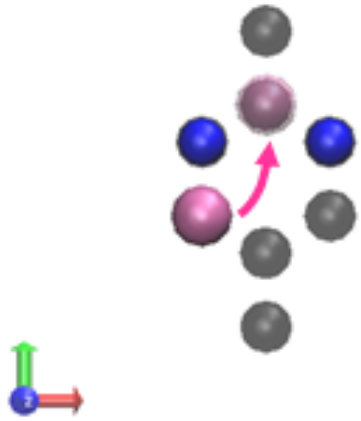

FIGURE 2.5 *Example of diffusion configurations of Boron on a graphene surface during the epitaxial growth*

By analyzing the bond number as well as the relative configurations before and after diffusion, we summarized 30 possible diffusion configurations for each kind of atom. **Fig.2.5** is an example of the diffusion processes. At the starting point, the Boron atom connects with one NN Nitrogen atom. After diffusion, it is surrounded by two Nitrogen atoms. Thus, we call this kind of diffusion as the B-1-2 diffusion. Due to the difference of relative locations of Boron and Nitrogen atoms, there are four kinds of B-1-2 diffusion configurations.

2.3 Calculation of energy barriers using Nudged Elastic Band (NEB) method

To obtain the energy barriers of adatom diffusion, we conducted first principle NEB calculations to simulate the diffusion processes. There exist infinite paths to transfer a

group of atoms from one stable configuration to another. However, the activation energy that each path needs to overcome, varies significantly. The aim of NEB method is to identify the minimum energy path (MEP), which is the atom diffusion routine with the lowest energy barrier.

The fundamental idea of NEB is to construct a set of equally separated images, usually 3 – 10, depending on the complexity of the system, between the initial and final states. The neighboring images are assumed to be connected by spring interaction, which ensures the continuity of the path [49]. In addition to the spring force between images, each image also experiences a true force resulting from the potential energy gradient. By optimizing the images to converge the total force of every images to zero, the NEB method is able to figure out the MEP.

The total force acting on image *i* is:

$$\vec{F}_i = \vec{F}_{potential\,,\perp} + \vec{F}_{spring,\parallel} \tag{2.6}$$

where

$$\vec{F}_{potential,\perp} = -\vec{\nabla}V(\vec{R}_i)|_\perp \tag{2.7}$$

$$\vec{F}_{spring,\parallel} = k_{i+1}\left(\vec{R}_{i+1} - \vec{R}_i\right) - k_i\left(\vec{R}_i - \vec{R}_{i-1}\right)|_\parallel \tag{2.8}$$

The original direction is referred to the line passing through the initial and end locations of the atom. $\vec{R}_i$ is the position vector of each image. $V(\vec{R}_i)$ refers to the potential energy of the image at position $\vec{R}_i$. k_i is the virtual spring constant between images. The total force is the combination of perpendicular component of the potential gradient and the

parallel component of the spring. The reason of neglecting the other part is to prevent 'corner cutting' and 'down-sliding' problems, which will pull the images off the MEP [49]. An example of optimizing initial guessed diffusion path to the MEP is shown in **Fig.2.6** [50].

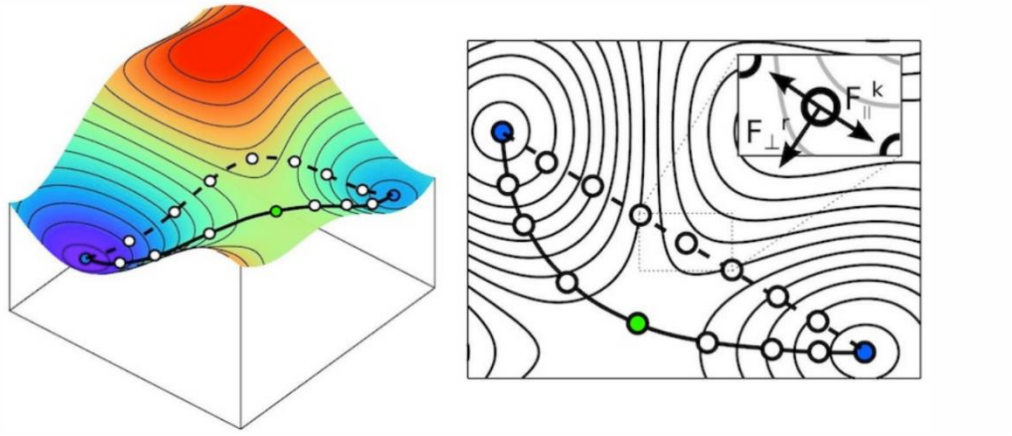

FIGURE 2.6 *Principle of NEB method. The dashed line is the initial guess of diffusion path. The continuous line is the optimized MEP, at which the green dot is the energy saddle point.* [50]

Diffusion barriers of various configurations are calculated using PWneb code from Quantum Espresso. The same pseudopotentials used total energy calculation were applied in energy barrier calculation. The quasi-Newton Broyden's second method is employed as the optimization scheme. The plane wave cut off energy is settled as 80 Ry. The converge threshold of the total force on images are defined to be 0.10 $eV/$Å. The initial guess path of MEP is defined by 7 equally separated intermediate images connected by virtual springs. The nudged elastic relaxations of projected forces via Verlet integration yields a discrete MEP. The energy barriers against diffusion,

adsorption, and desorption can be extracted from the saddle points on the MEP. **Fig.2.7** presents the diffusion energy barrier of B-2-3 (The Boron atom has 2 B-N bonds at the initial position and 3 B-N bonds at the end position), at which the saddle point locates at the 3rd image. According to the NEB calculation shown in **Fig 2.7**, the energy barrier of this B-2-3 configuration is 2.14 eV.

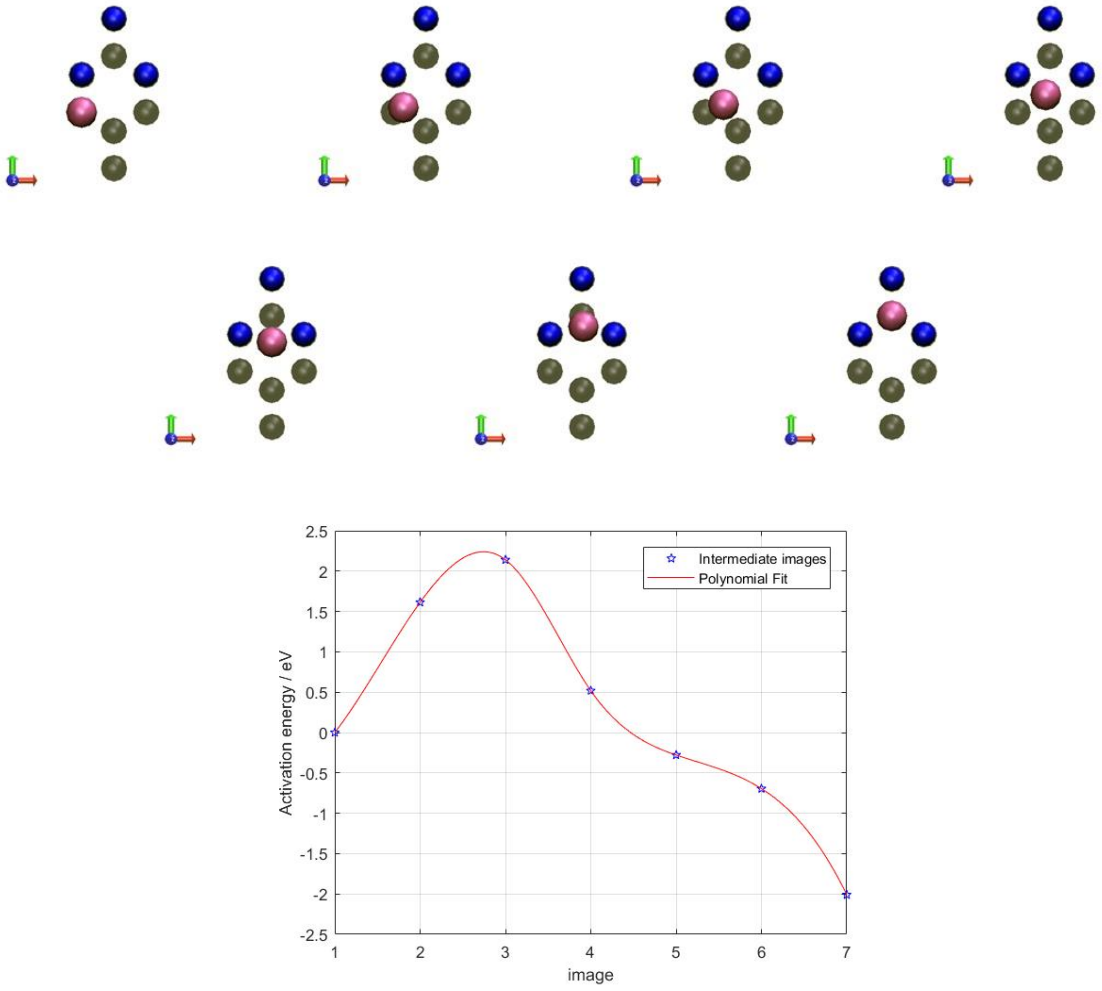

FIGURE 2.7 *Intermediate NEB images of B-2-3 surface diffusion configuration on graphene substrate, and Energy profile for B-2-3 surface diffusion configuration on graphene substrate using the nudged elastic band (NEB) method*

	0	**1**	**2**	**3**		
0	0.014	0.014	0.014		**1-1 Swing**	0.32
1	4.61	2.22	0.014	0.014	**Adsorption**	0.014
2	8.17	4.53	2.45	2.14	**Desorption**	0.78
3		7.28	4.15	2.56		

TABLE 2.3 *Energy barriers (eV) for epitaxial growth of Boron atoms on graphene substrate. The line number represents how many B-N bonds connects to the diffusion atom at the initial state, while the column number represents the number of bonds at the end state.*

	0	**1**	**2**	**3**		
0	0.018	0.018	0.018		**1-1 Swing**	0.39
1	4.61	2.15	0.018	0.018	**Adsorption**	0.018
2	5.41	4.12	2.81	1.86	**Desorption**	0.44
3		3.85	3.10	2.47		

TABLE 2.4 *Energy barriers (eV) for epitaxial growth of Nitrogen atoms on graphene substrate. The line number represents how many B-N bonds connects to the diffusion atom at the initial state, while the column number represents the number of bonds at the end state.*

The NEB calculation results indicate that the diffusion energy barriers are highly associated with the bond number differences between initial and end positions of the diffusing atom. A parameter *n* is defined to represent the bond number difference, where:

$$n = n(BN\ bonds)_{initial} - n(BN\ bonds)_{end} \quad (2.9)$$

A positive *n* means that there are more broken B-N bonds than formed bonds in the diffusion process, which usually results in a higher energy barrier. In most cases, for the diffusions with the same initial and end bond numbers, the energy barriers are usually analogous in every configuration, with a maximum difference of 0.05 eV. The only exception is the 1-1 atom swing which will be discussed later. Therefore, we assumed that, the diffusion barriers are only related with B-N bond numbers at the initial site and end site, and the relative position of Boron and Nitrogen does not affect the activation energy. This assumption makes it possible for us to simplify the model by combining configurations with same bond orders before and after diffusion. For each kind of adatom, there are 15 diffusion energy barriers, 1 adsorption energy barrier and 1 desorption energy barrier respectively. The tables of energy barriers are shown in **Table 2.3** and **Table 2.4**.

During the calculation, it is observed that, for B-1-1 and N-1-1, there exists a specific diffusion configuration, which presents a considerably lower barrier than other configurations with same initial and end states. The ordinary atom diffusion process and the specific process are referred as hopping and swing respectively. These two moves are shown schematically in **Fig.2.8.**

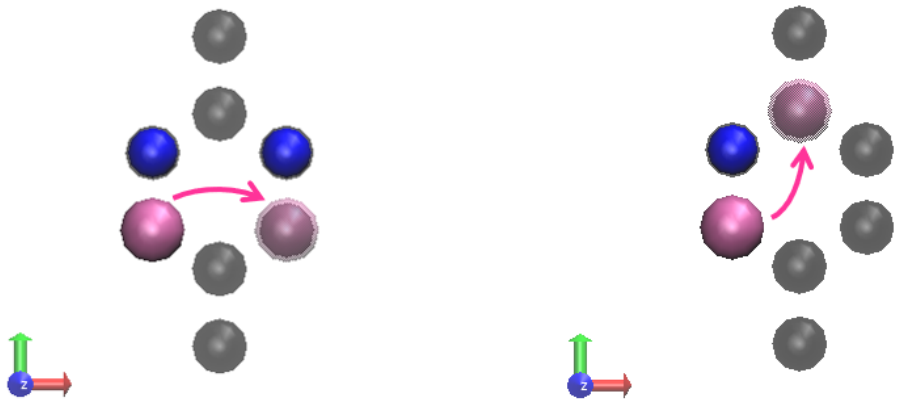

FIGURE 2.8 *Top view of hBN on graphene surface showing the Boron hopping and Boron swing. The Boron and Nitrogen atoms are shown as pink and blue.*

In **Fig.2.8**, the Boron atoms in both configurations have 1 B-N bond at the initial state and 1 B-N bond at the end state. In case of hopping moves, the Boron atom first detaches from its neighboring Nitrogen atom, then moves to its SNN site and forms bond with another Nitrogen atom. For the swing moves, the Boron atom keeps connected with the same Nitrogen atom and rotates to its nearby on-top site. The calculated diffusion barriers for Boron hopping is 2.22 eV, which is 1.90 eV higher than the swing energy barrier (0.32 eV). The same phenomenon is shared for Nitrogen atoms, where the energy barriers for 1-1 atom hopping and atom swing are 2.15 eV and 0.39 eV.

The cause of this variance is their difference at bond breaking process. Compared with the hopping move, the swing move does not involve bond breaking, which significantly reduces the activation energy for the diffusion process. This phenomenon strongly

affects the simulated growth configurations of hBN. The role of this discovery on the hBN growth morphology development will be investigated in detail in the Chapter 3.

CHAPTER 3

KMC SIMULATION OF HBN GROWTH ON HIGHLY ORDERED GRAPHENE LATTICES

3.1 KMC implementation and settings

Kinetic Monte Carlo (KMC) is a computational simulation method designed for modeling kinetic processes [35], [51], [52]. Unlike traditional Monte Carlo methods that study equilibrium conditions by the means of random numbers, a KMC model is capable of simulating dynamic processes [53]. In a KMC method, an event catalogue is constructed to list all possible kinetic moves in the system. For each event, a rate is assigned to describe its possibility of occurrence. The KMC system is quantized as a combination of stochastically sequenced events. During every step, an event is randomly selected from the catalogue, and the kinetic move represented by the event is applied in the system. Then, the catalogue of events is updated for the new configuration. These steps are repeated until the kinetic steady state is reached. The following steps explain the algorithm for the KMC method:

1. **Initiation:** analyze all possible events and calculate their rates r_i
2. **Cumulative rates:** list all possible events in the system, and calculate cumulative rate $\sum r_i$;
3. **Random sampling:** generate a random number $\varepsilon_1 \in [0,1)$, calculate a sampling parameter p, $p = \varepsilon_1 * \sum r_i$;

4. **Event selection:** loop through possible moves in the system until q th process, where

$$\sum_{i=1}^{q} r_i \leq p \leq \sum_{i=1}^{q+1} r_i \tag{3.1}$$

5. **Updating:** Proceed the selected event and updating the system configuration.
6. **Time advancement:** generate another random $\varepsilon_2 \in [0,1)$ and the real time advanced by Δt:

$$\Delta t = \frac{ln(\varepsilon_2)}{\sum r_i} \tag{3.2}$$

7. **Refreshing:** re-calculate the rates of all possible events r_i and cumulative rate $\sum r_i$ in the new configuration;
8. **Data collection:** collect the data;
9. **Convergence:** repeat step 3 to 8 until the system reaches real time bound;

In this study, the KMC method is used to simulate epitaxial growth of monolayer hBN on graphene substrate. The atom movements, including adsorption, diffusion and desorption, are defined as kinetic events. As discussed in last chapter, 15 diffusion events, 1 adsorption event and 1 desorption event were identified for each kind of atom. The event rates are obtained from the Arrhenius equation (**Eq 2.5**) based on transition state theory:

$$r = \nu_0 \exp(-\frac{E_B}{k_B T}) \tag{2.5}$$

The attempt frequency, ν_0, which correspond to the phonon frequency of an atom in a solid. For hBN, this prefactor is chosen as 10^{12} s^{-1} for both Boron and Nitrogen atoms. k_B is the Boltzmann constant and T is the growth temperature at the substrate surface. E_B is the barrier energy calculated from NEB method.

A KMC model is coded with Python 3.7, using *Numpy* and *random* package. At the beginning of each loop, the program will check all adatoms and their empty SNN sites to list all possible moves on the substrate. By counting the number of occupied NN sites around the adatom and its target SNN site, we can locate the energy barrier of the event in **Table 2.1** and **Table 2.2**. The rates of occurrence can be calculated by the Arrhenius equation. Then, random probing is utilized to samples event from the event catalogue. The selected move is proceeded on the configuration. The real time step Δt and total real time consumption $\sum \Delta t$ are updated to record real time duration. To simulate epitaxial deposition, an adatom will be added on a randomly chosen site every a constant real time interval. If the adatom is deposited on a site that has already been occupied, the atom will search for a suitable adsorption site amongst its SNN sites. If there present multiple choices, the target site will be selected randomly. In case all possible nearest diffusion sites have been occupied, the atom desorbs automatically, and the adsorption is regarded as having failed. The above procedures are repeated until the coverage of the graphene substrate reaches a preset percentage.

In this model, the impact of temperature, flux ratios and flux rates on hBN growth dynamics and propensities are simulated. The rates of events in the system are calculated by the Arrhenius equation, where temperature is involved. The flux ratios and flux rate influence adatom ratios and time interval between atom deposition. The temperature in the system is varied from 1450 K to 1650 K. The flux ratio is varied from N-rich to N-B equivalent to B-rich and the flux rate is varied from 0.001 ML/s to 0.1 ML/s, where 1 ML refers to 1 monolayer coverage.

A 32×64 sized KMC model is constructed with periodic boundary conditions in *x* and *y* directions. The Boron and Nitrogen atom are deposited randomly on the substrate and can diffuse to its SNN site. To capture accurate statistics of surface evolution, 60 trajectories are recorded in between that the surface coverage increases from 0 ML to 0.3 ML.

3.2 Surface growth morphology

3.2.1 Surface evolution in time

The surface morphology evolution versus time are presented in **Fig 3.1**. These graphs schematically show an example growth of hBN on 32 x 64 sized substrate under 1600 K, with the flux ratio of N : B = 1: 1 and the flux rate of 0.001 ML/s. A nucleus is defined as a collection of more than two connected adatoms. As can be observed in **Fig 3.1**, instead of isolated free atoms, the adatoms tend to join to form nuclei. Most nuclei transform to triangular shape as the deposition proceeds, which is a main feature of hcp lattices [52]. A majority of the triangular shaped nuclei are oriented in the same direction, which has been reported by many published researches of hBN MBE growth on different substrates [27], [54]. The nucleation process begins at the early stage of the growth, while afterwards, the nuclei formation rate reduced significantly. The nuclei size also grows as more atoms are deposited on the surface. In addition, it is noticed that the nuclei start coalescing with their neighbors to form bigger nuclei when the coverage

is greater than 0.16 ML. Such growth mode corresponds to the coarsening regime in a Frank–van der Merwe growth transition.

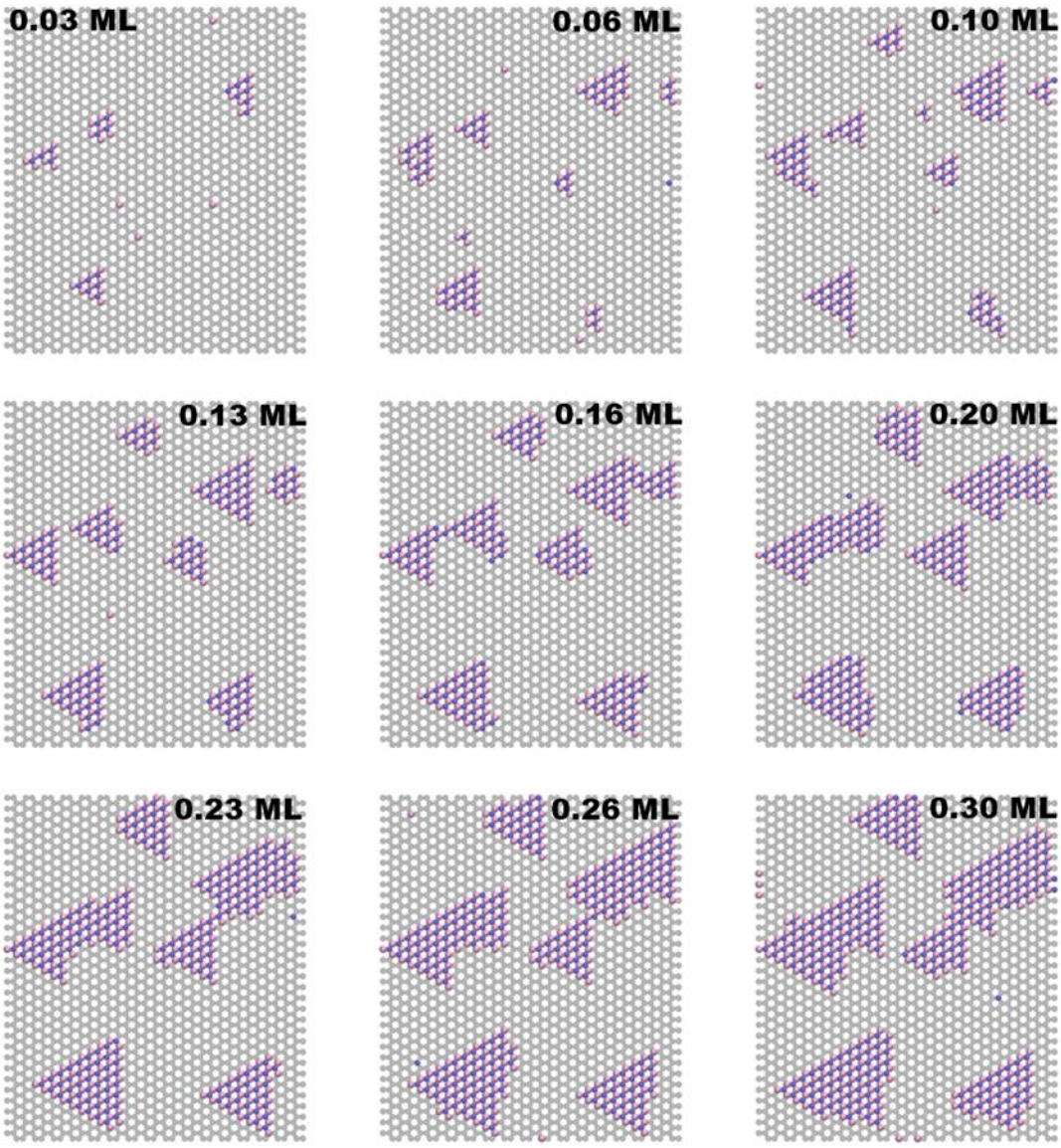

FIGURE 3.1 *hBN growth snapshots as a function of increasing coverage. The substrate size is* 32×64*, the temperature is 1600 K, the flux ratio is N : B = 1 : 1, and the flux rate is 0.001 ML/s. The sublayer represents graphene substrates, and the Boron and Nitrogen atoms are pink and blue respectively.*

3.2.2 Microscopic nuclei growth process

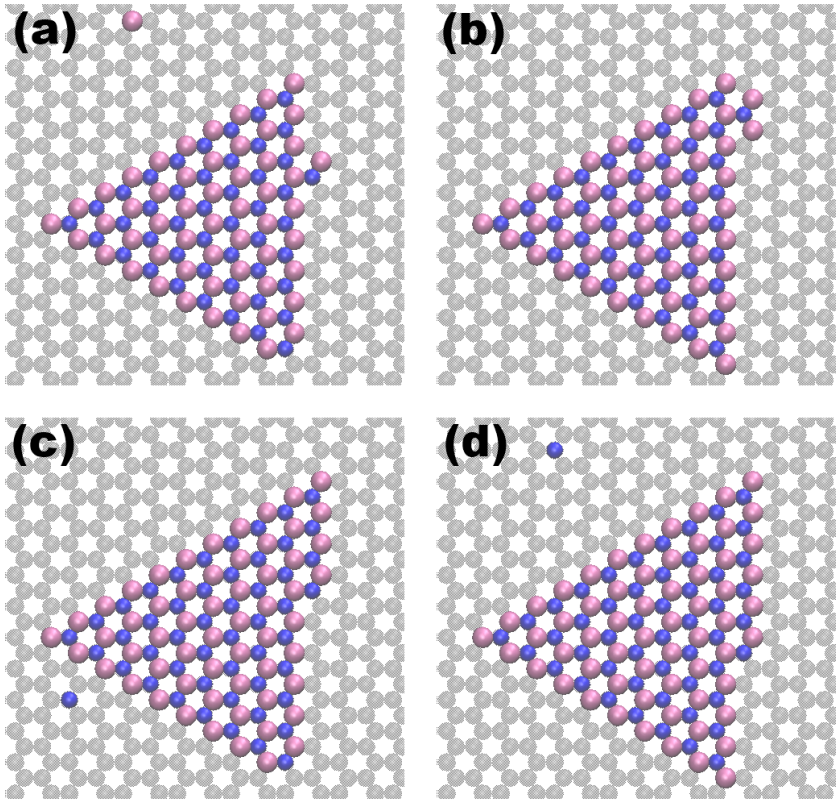

FIGURE 3.2 *Nucleus growth starting from step adatoms.* ***(a) – (d)*** *show the time-based surface growth evolution series.*

As shown in **Fig.3.2**, the hBN KMC model can simulate edge expansion growth mechanism of nucleus. In **Fig.3.2**, the first step of a nucleus growth is a sticking of an adatom on the nucleus ledge. As more atoms are deposited, free adatoms diffuse and connect with the step adatom. The new adatoms tend to diffuse to the sites near the nucleus edge because it can form more B-N bonds at these spots. The atom that stays in these spots are more stable due to the high diffusion energy barrier. Therefore, the nucleus expands along the edge as indicated in the simulation results. This edge

expansion growth mechanism is also predicted by the famous terrace-step-kink (TSK) model and has been observed in many thin film growth studies. [34], [51]

3.2.3 Defects observed in simulation

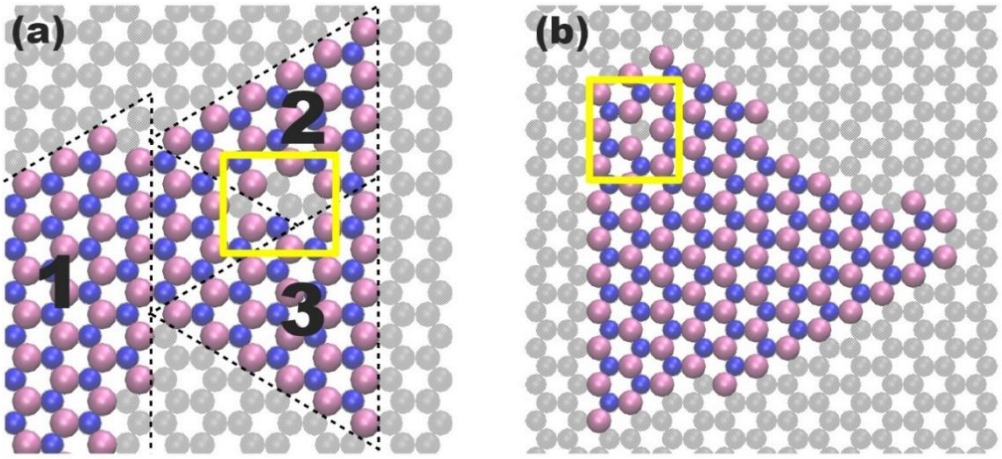

FIGURE 3.3 *Surface defects observed in simulation.* ***(a)*** *vacancies due to nuclei coalescence* ***(b)*** *Nitrogen vacancy*

During the simulation, two kinds of defects were observed on the growth surface. The first defect form, shown in **Fig.3.3 (a)**, is vacancies generated in nuclei coalescence. In most clustering process, the empty area between two nuclei will be slowly filled with adatoms. However, in some specific conditions, three nuclei merge together, leaving not enough steps to fill vacancies before adatom diffusion paths are blocked. Therefore, some vacancies are left inside the merged nuclei. The other kind of defect is single Nitrogen vacancy. This defect is caused by simultaneous edge extensions on the two edges near the vacancy site. The site is left unoccupied before the growing edges sealed the diffusion path.

3.3 Nucleation and growth rate

3.3.1 Nuclei density

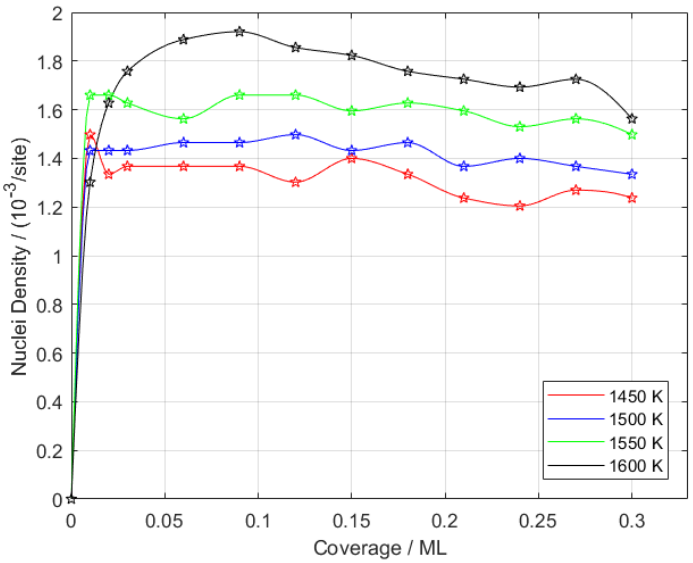

FIGURE 3.4 *Simulated hBN nuclei density as a function of surface coverage. The density increases with increased temperature (1450 K, 1500 K, 1550 K, and 1600 K), as displayed in different color. The flux ratio is N : B = 1 : 1 and the flux rate is 0.001 ML/s.*

During the KMC simulation, it is recognized that the hBN nuclei generation and growth follows some general regulations. Four regimes are defined to describe the level of hBN growth situations. The first regime (adatom regime) happens at the very beginning of the growth, when all deposited atoms on the substrate are unbonded atoms. As the coverage increases, the second regime, nucleation regime, starts when adatoms begin to aggregate together to form nuclei. During this regime, the nuclei density rises quickly and most nuclei are generated in this period. The next regime is called aggregation

regime, where the nucleation rate decreases, and the nuclei start to grow by absorbing adatoms. In the last regime, which is the combination regime, formation of new nuclei is rare as the adatoms tends to join in the existed nuclei. A slow drop of the nuclei density results from the nuclei integration.

The nuclei density at different coverage under various temperatures are counted and presented in **Fig.3.4**. The four growth regimes can be clearly located in the graph. Taking the growth at 1600 K as an example: the adatom regime is in 0 ML – 0.01 ML period, the nucleation regime is in 0.01 ML – 0.06 ML period, the aggregation regime is in 0.06 ML – 0.015 ML, and the combination regime starts afterwards. It can be observed in the figure that, nuclei density at different temperatures share the same tendency, even though the exact boundary between regimes may vary with respect to temperature.

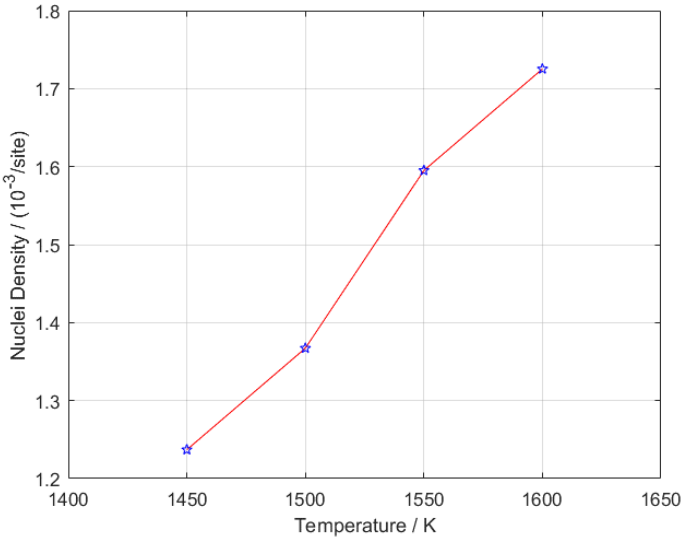

FIGURE 3.5 *Nuclei density as a function of deposition temperature. The coverage is 0.21 ML, the flux ratio is N : B = 1 : 1 and the flux rate is 0.001 ML/s.*

At the same coverage, the nuclei density increases as the growth temperature rises. This finding is coherent with the predictions from thin film growth theorem [55]. At higher temperature, the diffusion rate of adatoms is boosted, thus atoms collisions and reaction rate increase, resulting in more nuclei generation in the nucleation regime. **Fig.3.5** shows that hBN nuclei density increases roughly positive-linear dependent with respect to the growth temperature when the coverage is 0.21 ML

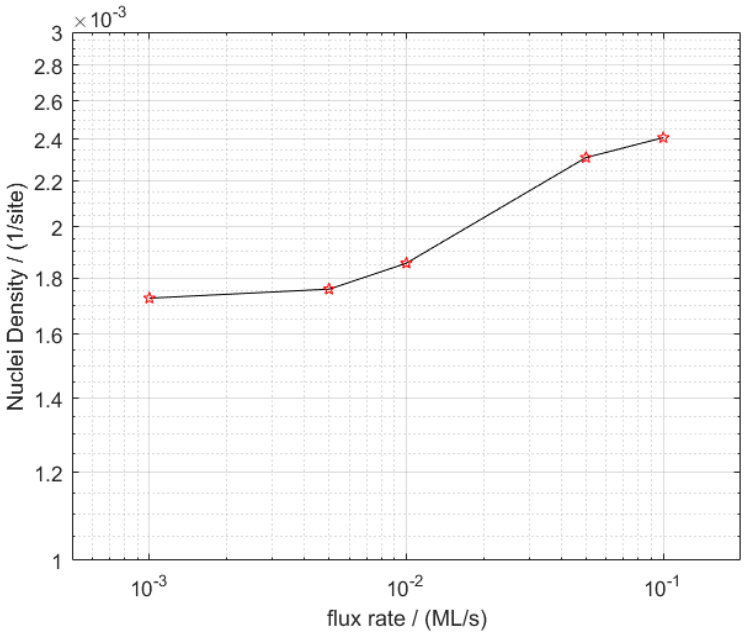

FIGURE 3.6 *Log scale plot of nuclei density as a function of flux rate at 0.21 ML. The growth temperature is 1600 K and the flux ratio is N : B = 1 : 1*

The relationship between average surface nuclei density and the input flux rate are shown in **Fig 3.6**. It can be observed that rapid input flux will lead to denser surface nuclei. This is because the increase of flux rate brings about more adatoms on the deposition surface in a time unit. Thus, the adatoms collision rate at nucleation regime grows higher, which elevates the nucleation rate and promotes the nuclei density.

3.3.2 Coverage growth rate

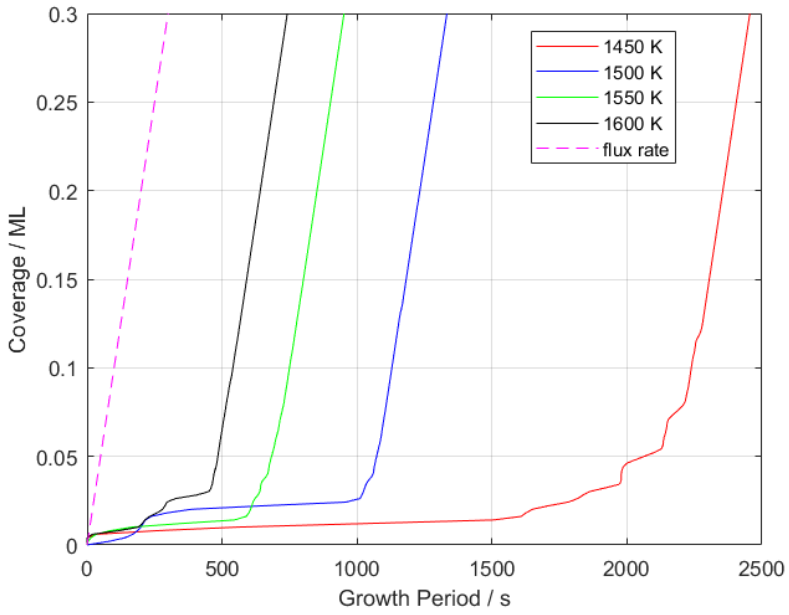

FIGURE 3.7 *Simulated hBN growth rate under 1450 K, 1500 K, 1550 K and 1600 K. The flux ratio is N : B = 1 : 1 and the flux rate is 0.001 ML/s. The input flux rate is also drawn in dashed pink line.*

To study the hBN growth rate, we calculated and plotted the substrate coverage with respect to real time change in the KMC simulation in **Fig.3.7**. The results indicate that the growth rate at low coverage (< 0.03 ML) is much smaller than input flux rate. When the coverage surpasses a threshold, which is around 0.03 ML, the growth rate accelerates quickly and converge to the flux rate.

The reason of low growth rate at early deposition stage is the adatom desorption and N_2 evaporation. To simulate the real growth situations, desorption move is added to the

KMC event catalogue for both Boron and Nitrogen free adatoms. In addition, we also considered the Nitrogen molecule formation and evaporation moves, when two unbonded Nitrogen adatoms are at each other's SNN site. Before the coverage reaches 0.03 ML, the growth model is in the adatom regime, where most deposited atoms are free adatoms and are likely to desorb from the surface. As more atoms are deposited on the surface, the nucleation process emerges, which combines adatoms together. The grown nuclei provide more connection sites with expanded edges, which will capture more unbonded adatoms. This positive feedback circle leads to a sharp decline of free atoms on the substrate. As a result, the growth rate rises until it converges to the flux rate.

Fig 3.7 also reveals that the temperature increment will lead the growth rate to converge faster. As discussed above, a more intensive nuclei density is expected for higher growth temperature. At the same time, more nuclei attract more adatoms to be bonded on the nuclei edge and promote the convergence of nuclei rate.

3.4 Impact of flux ratio

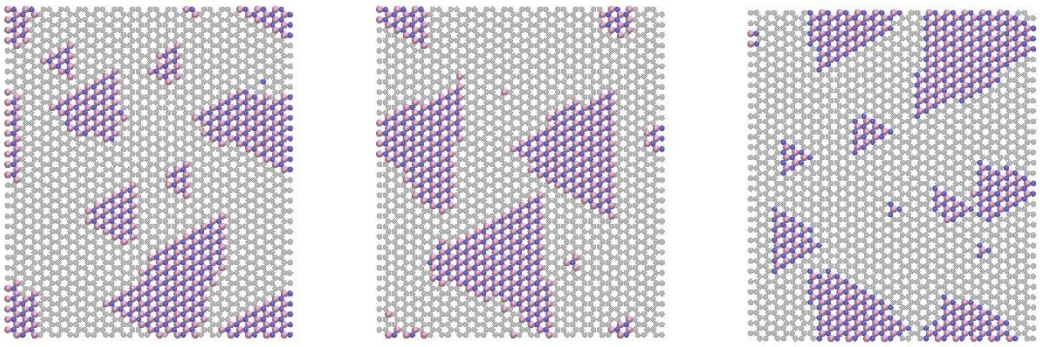

FIGURE 3.8 *Surface morphology at different flux ratio* ***(a)*** *N : B = 0.8 : 1* ***(b)*** *N : B = 1 : 1* ***(c)*** *N : B = 1.2 : 1. The coverage is 0.3 ML, the temperature is 1450 K and the flux rate is 0.001 ML/s*

In **Fig 3.8**, the surface morphology of hBN grown under different flux ratio is presented. Triangular shaped flakes are observed in all conditions. However, the orientation of flake directions varies in accordance with the N:B input ratio. When the input flux ratio is B-rich or Nitrogen and Boron are equivalent, the top-angle of hBN flake points to the top-right. When the input flux ratio is N-rich, the top-angle of hBN flake points to the top-left. Since N atom has lower desorption energy barrier and can form gaseous N_2 to evaporate, the remaining N atoms on surface are usually less than B atoms at N-B equivalent condition. Therefore, in most cases, N-B equivalent simulations are desorption-caused B-rich condition, which results in similar configurations as B-rich conditions. In addition, the terminal atom type of the hBN flakes is determined by the input flux ratio. The terminal atom is defined at the atom type of the edge atoms of the flake. Atoms with more intensive density are more likely to become the terminal atoms

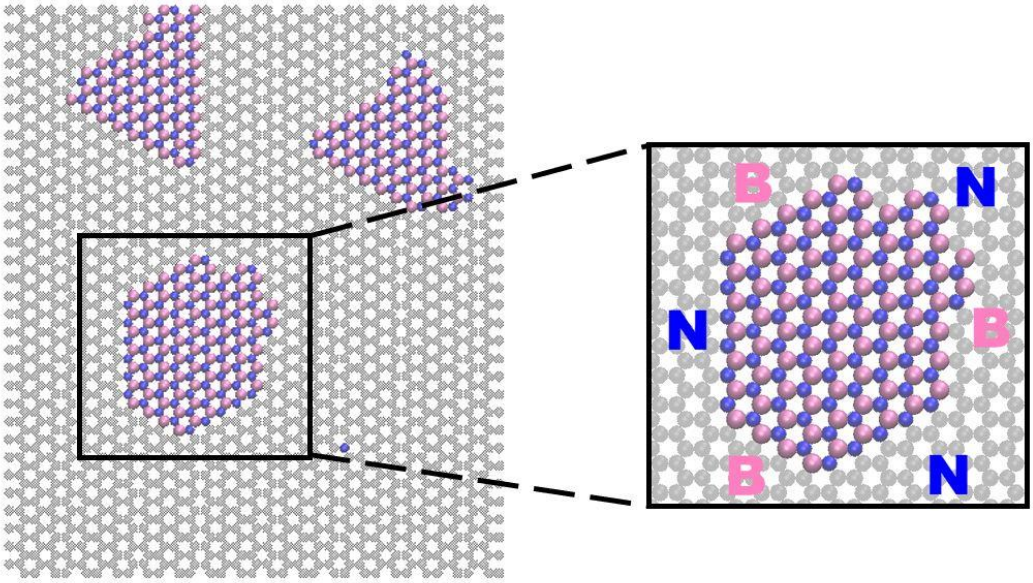

FIGURE 3.9 *Hexagonal shaped hBN island, the terminal atom types are shown. The coverage is 0.3 ML, the temperature is 1450 K, the flux rate is 0.001 ML/s and the flux ratio is N : B = 1 : 1*

of the flakes. Except for the triangular shaped hBN flake, the hexagonal islands are also detected when the input flux ratio is around N: B = 1: 1. Under N-B equivalent conditions, there may not be a dominant edge type. As shown in **Fig 3.9**, the hexagonal shaped hBN island has both B-terminal edges and N-terminal edges. Each terminal type has three edges and different terminal edges are separately distributed. If the terminal edges of the same type are elongated to intersect, triangular shaped flakes will be recognized. For these imagined triangular flakes, they have the same direction orientations as their respective atom rich conditions. During the hexagonal island grown process, it is also noticed that the B edge and N edge are under competition. Either type tries to compensate the other type to form a triangle of its own orientation. However,

the equivalent input ratio protects the balanced hexagonal shape from transformation. Thus, a conclusion can be made that the flux ratio is responsible for the shape and orientation of the epitaxial grown hBN flake in a way of controlling the terminal atom types.

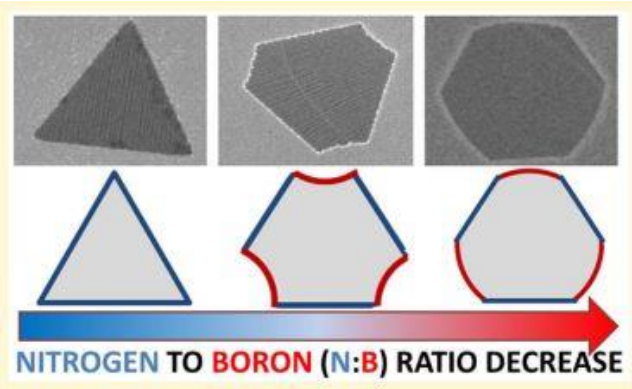

FIGURE 3.11 *The surface morphology of CVD grown hBN on copper surface. Showing the shape transformation of hBN flake with respect to N: B ratio.* [54]

The relationship between input flux ratio and hBN flake shape has been confirmed by Stehle et al. [54]. According to **Fig 3.11**, all three shapes contain at least three Nitrogen edges, which are identified in blue color. The morphology of single domains changes from triangular to truncated triangular and finally pseudo hexagonal shape as the N: B ratio decreases. It is believed that the decreased available active Nitrogen affects the N-edge growth rate and results in appearance of B-rich edges, which changes the crystal shape gradually. Their experimental results support our prediction and prove the reliability of our KMC model to simulate the real MBE growth. In addition, the KMC model theoretically explains the growth mechanism of hexagonal shaped hBN flake and reveals the competitive relationship between two edge types.

3.5 Impact of atom swing

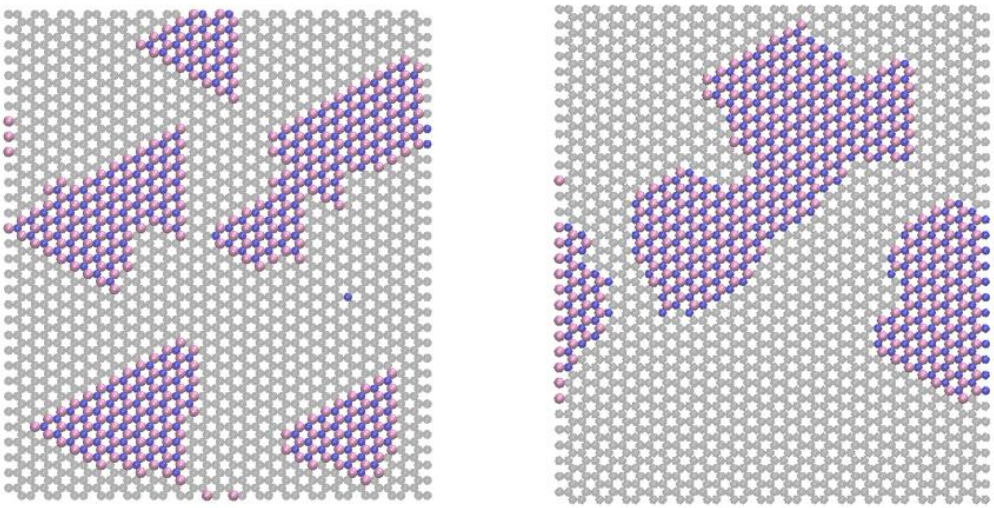

FIGURE 3.12 *Surface morphologies for with and without atom swing. The coverage is 0.3 ML, the temperature is 1600 K, the flux rate is 0.001 ML/s and the flux ratio is N : B = 1 : 1*

Atom swing is a special 1-1 atom diffusion move, because it does not involve B-N bond breaking. Compared with 1-1 atom hopping, the atom swing has significantly lower diffusion energy barrier. To show the influence of atom swing in shaping the hBN flakes, we performed KMC simulations for the MBE growth of hBN with and without the special atom move. The surface morphologies of hBN flakes with and without atom swing move are presented in **Fig 3.12**. The surface morphologies show that the flakes are more triangular when atom swing is considered in the simulation. The atom swing process enables 1-1 connected N and B atoms to rotate at relatively lower energy barrier, which increases the choices of atoms diffusion targets and increases their opportunity to diffuse to more stable locations.

CHAPTER 4

THEORETICAL CALCULATION OF N-ISOTOPES RATIO AND THICKNESS INDUCED HBN RAMAN PEAK SHIFT

4.1 Model construction and optimization

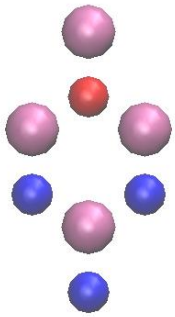

FIGURE 4.1 *Relaxed isotopic hBN unit cell. The B, N^{14}, and N^{15} are represented by pink, blue and red. This model simulates the hBN monolayer grown with 25% N^{15}.*

To calculate the phonon signature of hBN, the first step is to construct and optimize its unit cell model. Based on the relaxed hBN-Graphene heterostructure from Chapter 2, the initial guess of monolayer hBN^{14} and hBN^{15} primitive unit cells on graphite substrates are constructed according to the cell parameter and atomic position data from **Table 2.1** and **Table 2.2**. In order to calculate the impact of N isotope ratio on hBN Raman peaks, a hBN unit cell model with four primitive unit cells were built, and the structure is shown in **Fig 4.1**. This model has periodic boundaries to simulate an infinite hBN monolayer on a graphite substrate. The pink atoms represent Boron atom. The blue

and red atoms represent N^{14} and N^{15} atoms respectively. By altering the relative numbers of N isotopes in the model, we can simulate the hBN films grown under various N isotope ratios. Five models, with 0%, 25%, 50%, 75%, and 100% N^{15}, were constructed.

FIGURE 4.2 *Top view and cross view of a tri-layer hBN structure*

Apart from the isotopic effect, the impact of thickness was also taken into consideration. **Fig 4.2** shows the top view and cross view of a tri-layer hBN unit cell. For the hBN films grown with N isotopes, single, double, and triple layer hBN model were constructed and optimized. The relaxation follows the same steps as discussed in Chapter 2. The plane wave kinetic energy cutoff of the valence electrons is 80 Ry. Exchange correlation energy was treated with the generalized gradient approximation (GGA). The Perdew-Burke-Ernzerhof (PBE) functional was used in combination with Vanderbilt ultrasoft pseudopotentials for B, C and N atoms. The self-consistent convergence threshold was set to be 10^{-8} eV.

After relaxation, the lattice constant of monolayer and few layers hBN are optimized to 2.488 Å and 2.498 Å respectively. The c-direction of these unit cell models were set to be 20 Å to minimize the interactions between perpendicular images.

4.2 Raman shift hBN synthesized with N^{14} and N^{15} isotopes

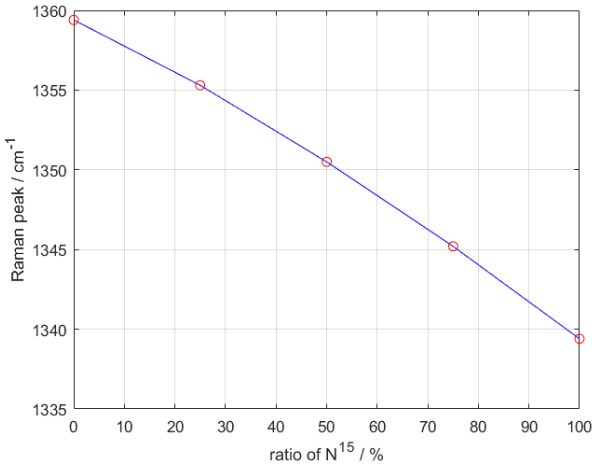

FIGURE 4.3 *Gamma band Raman peaks of hBN grown with different ratio of N^{15}*

To understand the isotopic effect on the gamma band Raman signatures, the first principle DFT calculation of monolayer hBN, with different N isotope ratios, was conducted. The kinetic energy for wavefunctions and the threshold for self-consistence were set to be 80 Ry and 10^{-16} eV. A gamma-centered $8 \times 8 \times 1$ k-grid was selected to sample the Brillouin zone.

For monolayer hBN on grown on graphite substrate, the calculated Raman peak at gamma band locates at 1359.4 cm^{-1} for pure N^{14} and 1339.4 cm^{-1} for pure N^{15}. As shown in **Fig 4.3**, the frequency of gamma band Raman peaks of hBN decreased with increased

N^{15} ratio. The Raman peak is the frequency of phonons, which follows the rule of harmonic oscillation:

$$f \propto \sqrt{\frac{k}{m}} \tag{4.1}$$

Thus, the substitution of N^{14} with N^{15} increases the atomic mass and results in a decrement of the Raman peaks. The prediction is in agreement with the experimental results from Ryan Page and Dr. Yongjin Cho.

The experimental Raman peaks of hBN grown with N^{14} and N^{15} is at 1360.8 cm^{-1} and 1346.4 cm^{-1}. It can be observed that our simulation results are downshifted relative to experimental values. This error may come from our assumption that the hBN lattices are all constrained to match the hexagonal shaped graphite surface. In reality, there might be defect on between the hBN films and graphite substrate, which release the strain of hBN and cause the Raman peak shift. Our model can be further improved by taking them into consideration.

4.3 Raman shift of multiple layer hBN grown with N^{14}/N^{15}

	Raman peaks (N^{14}) / cm^{-1}	Raman peaks (N^{15}) / cm^{-1}
1	1359.4	1339.4
2	1357.4	1338.2
3	1356.5	1337.7
Bulk	1356.8 [56]	NA

TABLE 4.1 *Gamma band Raman peak of multiplayer hBN grown with N^{14} and N^{15}*

In this section, we calculated the thickness induced gamma band Raman peak shift of hBN. The DFT PHonon calculation were performed on single, bilayer, tri-layer hBN models with pure N^{14} and pure N^{15}. The parameters in the experiments are the same as the values in the last part.

The results, presented in **Table 4.1**, indicate that the Raman peak of hBN drops as the thickness of hBN films increases. This trend is also observed in many other 2D materials [38], [39], [57]. However, comparing to the Raman signature of graphene and MoS_2, the values of hBN does not depend sensibly on the layers number.

CHAPTER 5

CONCLUSION

In this work, a lattice-based Kinetic Monte Carlo model, combined with the first principle Density Functional Theory, was utilized to illustrate the epitaxial growth principles of hexagonal Boron Nitride on highly ordered graphite substrate. We first drew the total energy map of B/N atoms on graphene primitive unit cell and revealed that the on-top site is the most stable location for both B and N adsorbed adatoms on the graphite surface. The hBN-Graphene heterostructure were relaxed to obtain its optimized cell parameters and atomic positions. We analyzed all possible diffusion configurations and calculated the energy barriers based on Nudged Elastic Band theory. We recognized that the diffusion energy barrier increases as more B-N bonds are broken during the diffusion process. After figuring out the decisive effect of initial and end bond numbers on the value of energy barrier, the diffusion configurations were simplified to 15 conditions for each kind of adatom. The 1-1 atom swing is an interesting diffusion movement, where it has the same initial and end bond numbers as 1-1 atom hopping but has significantly lower energy barrier. The KMC model of hBN epitaxial growth on graphite substrate was constructed based on the above DFT calculation results. The hBN surface evolution in time was successfully simulated which is in accordance with experimental results. The atomic level growth mechanism on the substrate follow the famous terrace-step-kink model. Some traditional defects of hBN layers, such as N vacancies, were observed in the simulation. By analyzing the surface morphology, we found out that both increased flux rate and temperature will lead to an

increase in nuclei density at early stage hBN growth, as a result of the more frequent atomic collisions. It is also discovered that at low coverage, the input flux rate is much higher than the hBN coverage growth rate, which accelerates quickly and converges to the input flux rate when the coverage exceeds 0.05 ML. The convergence is achieved faster at higher surface temperature. The flux ratio is responsible for the shape and orientation of the hBN flake in a way of controlling the type of terminal edge atoms. In addition, the shape of hBN flake will be more triangular if the atom swing is considered in the simulation. In the next part, we evaluated the N isotopes and thickness induced Raman peak shift of hBN films grown on graphite substrate. The multilayer hBN models with different N^{15} ratios were constructed with the help of first principle relaxation. The calculated monolayer hBN Raman peak at E_{2g} mode is 1359.4 cm^{-1} for pure N^{14} and 1339.4 cm^{-1} for pure N^{15}. Both increasing the N^{15} ratio and the number of hBN layers lead to decreased phonon frequency of gamma band Raman peak.

REFERENCES

[1] A. K. Geim and K. S. Novoselov, "The rise of graphene," *Nat. Mater.*, vol. 6, pp. 183–191, 2007.

[2] K. F. Mak, C. Lee, J. Hone, J. Shan, and T. F. Heinz, "Atomically thin MoS2: A new direct-gap semiconductor Kin," *Phys. Rev. Lett.*, vol. 105, 2010.

[3] B. Radisavljevic, A. Radenovic, J. Brivio, V. Giacometti, and A. Kis, "Single-layer MoS2 transistors," *Nat. Nanotechnol.*, vol. 6, no. 3, pp. 147–150, 2011.

[4] A. Splendiani *et al.*, "Emerging photoluminescence in monolayer MoS 2," *Nano Lett.*, vol. 10, no. 4, pp. 1271–1275, 2010.

[5] X. Wang, H. Feng, Y. Wu, and L. Jiao, "Controlled synthesis of highly crystalline MoS2 flakes by chemical vapor deposition," *J. Am. Chem. Soc.*, vol. 135, no. 14, pp. 5304–5307, 2013.

[6] M. O. Li, D. Esseni, J. J. Nahas, D. Jena, and H. G. Xing, "Two-dimensional heterojunction interlayer tunneling field effect transistors (Thin-TFETs)," *IEEE J. Electron Devices Soc.*, vol. 3, no. 3, pp. 200–207, 2015.

[7] A. J. Mannix *et al.*, "Synthesis of borophenes: Anisotropic, two-dimensional boron polymorphs," *Science (80-.).*, vol. 350, no. 6267, pp. 1513–1516, 2015.

[8] I. Naumov, A. M. Bratkovsky, and V. Ranjan, "Unusual flexoelectric effect in two-dimensional noncentrosymmetric sp2-bonded crystals," *Phys. Rev. Lett.*, vol. 102, no. 21, pp. 2–5, 2009.

[9] S. Dai *et al.*, "Subdiffractional focusing and guiding of polaritonic rays in a natural hyperbolic material," *Nat. Commun.*, vol. 6, no. 1, pp. 6963–6963, 2015.

[10] C. R. Dean *et al.*, "Boron nitride substrates for high-quality graphene electronics," *Nat. Nanotechnol.*, vol. 5, no. 10, pp. 722–726, 2010.

[11] K. K. Kim *et al.*, "Synthesis of monolayer hexagonal boron nitride on Cu foil using chemical vapor deposition," *Nano Lett.*, vol. 12, no. 1, pp. 161–166, 2012.

[12] H. X. Jiang and J. Y. Lin, "Hexagonal boron nitride for deep ultraviolet photonic devices," *Semicond. Sci. Technol.*, vol. 29, no. 8, 2014.

[13] T. T. Tran *et al.*, "Quantum Emission from Defects in Single-Crystalline Hexagonal Boron Nitride," *Phys. Rev. Appl.*, vol. 5, no. 3, pp. 2–6, 2016.

[14] K. Ahmed, R. Dahal, A. Weltz, J. Q. Lu, Y. Danon, and I. B. Bhat, "Growth of hexagonal boron nitride on (111) Si for deep UV photonics and thermal neutron detection," *Appl. Phys. Lett.*, vol. 109, no. 11, pp. 1–5, 2016.

[15] K. Zhang, Y. Feng, F. Wang, Z. Yang, and J. Wang, "Two dimensional hexagonal boron nitride (2D-hBN): Synthesis, properties and applications," *J. Mater. Chem. C*, vol. 5, no. 46, pp. 11992–12022, 2017.

[16] Y. Zeng *et al.*, "High-Quality Magnetotransport in Graphene Using the Edge-Free Corbino Geometry," *Phys. Rev. Lett.*, vol. 122, no. 13, pp. 3–8, 2019.

[17] M. Yankowitz, Q. Ma, P. J. Herrero, and B. J. LeRoy, "van der Waals heterostructures combining graphene and hexagonal boron nitride," *Nat. Rev. Phys.*, vol. 1, pp. 112–125, 2019.

[18] A. Nagashima, N. Tejima, Y. Gamou, T. Kawai, and C. Oshima, "Electronic structure of monolayer hexagonal boron nitride physisorbed on metal surfaces," *Phys. Rev. Lett.*, vol. 75, no. 21, pp. 3918–3921, 1995.

[19] L. Ci *et al.*, "Atomic layers of hybridized boron nitride and graphene domains," *Nat. Mater.*, vol. 9, no. 5, pp. 430–435, 2010.

[20] J. Xue *et al.*, "Scanning tunnelling microscopy and spectroscopy of ultra-flat graphene on hexagonal boron nitride," *Nat. Mater.*, vol. 10, no. 4, pp. 282–285, 2011.

[21] J. Martin *et al.*, "Observation of electron-hole puddles in graphene using a scanning single-electron transistor," *Nat. Phys.*, vol. 4, no. 2, pp. 144–148, 2008.

[22] P. Maher *et al.*, "Evidence for a spin phase transition at charge neutrality in bilayer graphene," *Nat. Phys.*, vol. 9, no. 3, pp. 154–158, 2013.

[23] R. Page, Y. Cho, J. Casamento, S. Rouvimov, H. G. Xing, and D. Jena, "Rotationally aligned hexagonal boron nitride on sapphire by high-temperature molecular beam epitaxy," *Phys. Rev. Mater.*, vol. 3, no. 6, 2019.

[24] Q. S. Paduano, M. Snure, and J. Shoafy, "Effect of V/III ratio on the growth of hexagonal boron nitride by MOCVD," *Mater. Res. Soc.*, vol. 1726, no. 1557, pp. 83–88.

[25] H. Park, T. K. Kim, S. W. Cho, H. S. Jang, S. I. Lee, and S. Y. Choi, "Large-scale synthesis of uniform hexagonal boron nitride films by plasma-enhanced atomic layer deposition," *Sci. Rep.*, vol. 7, no. 1, pp. 40091–40091, 2017.

[26] H. I. Rasool, C. Ophus, and A. Zettl, "Atomic Defects in Two Dimensional Materials," *Adv. Mater.*, vol. 27, no. 38, pp. 5771–5777, 2015.

[27] G. I. López-Morales, N. V. Proscia, G. E. López, C. A. Meriles, and V. M. Menon, "Toward the Identification of Atomic Defects in Hexagonal Boron

Nitride: X-Ray Photoelectron Spectroscopy and First-Principles Calculations," vol. 1, no. Cvd, pp. 1–5, 2018.

[28] G. Kresse and J. Furthmüller, "Efficient iterative schemes for ab initio total-energy calculations using a plane-wave basis set," *Phys. Rev. B*, vol. 54, no. 16, pp. 11169–11186, 1996.

[29] J. P. Perdew, K. Burke, and M. Ernzerhof, "Generalized Gradient Approximation Made Simple - The PBE functional," *Phys. Rev. Lett.*, vol. 77, no. 18, pp. 3865–3868, 1996.

[30] G. Kresse and D. Joubert, "From ultrasoft pseudopotentials to the projector augmented-wave method," *Phys. Rev. B*, vol. 59, no. 3, pp. 1758–1775, 1999.

[31] N. Metropolis, A. W. Rosenbluth, M. N. Rosenbluth, and A. H. Teller, "Equation of State Calculations by Fast Computing Machines," *J. Chem. Phys.*, vol. 21, no. 6, pp. 1087–1092, 1953.

[32] R. Whitesides and M. Frenklach, "Detailed kinetic Monte Carlo simulations of graphene-edge growth.," *J. Phys. Chem. A*, vol. 114, no. 2, pp. 689–703, 2010.

[33] Y. Nie *et al.*, "First principles kinetic Monte Carlo study on the growth patterns of WSe_2 monolayer," *2D Mater.*, vol. 3, no. 2, p. 025029, 2016.

[34] A. Govind Rajan, J. H. Warner, D. Blankschtein, and M. S. Strano, "Generalized Mechanistic Model for the Chemical Vapor Deposition of 2D Transition Metal Dichalcogenide Monolayers," *ACS Nano*, vol. 10, no. 4, pp. 4330–4344, 2016.

[35] Y. Nie, C. Liang, P.-R. Cha, L. Colombo, R. M. Wallace, and K. Cho, "A kinetic Monte Carlo simulation method of van der Waals epitaxy for atomistic

nucleation-growth processes of transition metal dichalcogenides," *Sci. Rep.*, vol. 7, no. 1, p. 2977, 2017.

[36] C. Gong, L. Colombo, R. M. Wallace, and K. Cho, "The unusual mechanism of partial fermi level pinning at metal-MoS 2 interfaces," *Nano Lett.*, vol. 14, no. 4, pp. 1714–1720, 2014.

[37] Z. Ni, Y. Wang, T. Yu, and Z. Shen, "Raman spectroscopy and imaging of graphene," *Nano Res.*, vol. 1, no. 4, pp. 273–291, 2008.

[38] H. Li *et al.*, "From bulk to monolayer MoS 2: Evolution of Raman scattering," *Adv. Funct. Mater.*, vol. 22, no. 7, pp. 1385–1390, 2012.

[39] Z. H. Ni, T. Yu, Y. H. Lu, Y. Y. Wang, Y. P. Feng, and Z. X. Shen*, "Uniaxial Strain on Graphene: Raman Spectroscopy Study and Band-Gap Opening," *ACS Nano*, vol. 2, no. 1, pp. 2301–2305, 2008.

[40] A. Das *et al.*, "Monitoring dopants by Raman scattering in an electrochemically top-gated graphene transistor," *Nat. Nanotechnol.*, vol. 3, no. 4, pp. 210–215, 2008.

[41] Y. You, Z. Ni, T. Yu, and Z. Shen, "Edge chirality determination of graphene by Raman spectroscopy," *Appl. Phys. Lett.*, vol. 93, no. 16, pp. 23–25, 2008.

[42] F. J. Manjón *et al.*, "Effect of N isotopic mass on the photoluminescence and cathodoluminescence spectra of gallium nitride," *Eur. Phys. J. B*, vol. 40, no. 4, pp. 453–458, 2004.

[43] M. Asen-Palmer *et al.*, "Thermal conductivity of germanium crystals with different isotopic compositions," *Phys. Rev. B - Condens. Matter Mater. Phys.*, vol. 56, no. 15, pp. 9431–9447, 1997.

[44] K. M. Itoh and E. E. Haller, “Isotopically engineered semiconductors - New media for the investigation of nuclear spin related effects in solids,” *Phys. E Low-Dimensional Syst. Nanostructures*, vol. 10, no. 1–3, pp. 463–466, 2001.

[45] T. Q. P. Vuong *et al.*, “Isotope engineering of van derWaals interactions in hexagonal boron nitride,” *Nat. Mater.*, vol. 17, no. 2, pp. 152–158, 2018.

[46] W. Q. Han *et al.*, “Isotope effect on band gap and radiative transitions properties of boron nitride nanotubes,” *Nano Lett.*, vol. 8, no. 2, pp. 491–494, 2008.

[47] O. Hod, “Graphite and Hexagonal Boron-Nitride Possess the Same Interlayer Distance. Why?,” *J. Chem. Theory Comput.*, vol. 8, no. 4, pp. 1360–1369, 2012.

[48] N. Ueda, H. Hosono, R. Waseda, and H. Kawazoe, “Synthesis and control of conductivity of ultraviolet transmitting β-Ga2O3single crystals,” *Appl. Phys. Lett.*, vol. 70, no. 26, pp. 3561–3563, 1997.

[49] H. Jonsson, G. Mills, and K. W. Jacobsen, “Nudged elastic band method for finding minimum energy paths of transitions,” *J. Chem. Phys.*, vol. 142, no. 2, pp. 024106–024106, 2015.

[50] G. Henkelman, “Methods for Calculating Rates of Transitions with Application to Catalysis and Crystal Growth,” 2001.

[51] F. Grosse and R. Zimmermann, “Monte Carlo growth simulation for Al(x)Ga(1-x)As heteroepitaxy,” vol. 212, pp. 128–137, 2000.

[52] M. Chugh and M. Ranganathan, “Lattice kinetic Monte Carlo simulation study of the early stages of epitaxial GaN (0001) growth,” *Appl. Surf. Sci.*, vol. 422,

pp. 1120–1128, 2017.

[53] F. Krzyżewski and M. A. Załuska-Kotur, “Stability diagrams for the surface patterns of GaN(0001¯) as a function of Schwoebel barrier height,” *J. Cryst. Growth*, vol. 457, pp. 80–84, 2017.

[54] Y. Stehle *et al.*, “Synthesis of Hexagonal Boron Nitride Monolayer: Control of Nucleation and Crystal Morphology,” *Chem. Mater.*, vol. 27, no. 23, pp. 8041–8047, 2015.

[55] M. Ohring, *The materials science of thin films*, no. c. 1992.

[56] Q. Cai *et al.*, “Raman signature and phonon dispersion of atomically thin boron nitride,” *Nanoscale*, vol. 9, no. 9, pp. 3059–3067, 2017.

[57] C. Androulidakis, E. N. Koukaras, M. Poss, K. Papagelis, C. Galiotis, and S. Tawfick, “Strained hexagonal boron nitride: Phonon shift and Grüneisen parameter,” *Phys. Rev. B*, vol. 97, no. 24, 2018.